

# Trade-off between optical modulation amplitude and modulation bandwidth of silicon micro-ring modulators

Hui Yu,<sup>1</sup> Diqing Ying,<sup>2,\*</sup> Marianna Pantouvaki,<sup>3</sup> Joris Van Campenhout,<sup>3</sup> Philippe Absil,<sup>3</sup> Yinlei Hao,<sup>1</sup> Jianyi Yang,<sup>1</sup> and Xiaoqing Jiang<sup>1</sup>

<sup>1</sup>Institute of Microelectronics and Optoelectronics, Department of Information Science and Electronic Engineering, Zhejiang University, Hangzhou 310027, China

<sup>2</sup>Micro-Satellite Research Center, Zhejiang University, Hangzhou 310027, China

<sup>3</sup>imec, Kapeldreef 75, 3001 Leuven, Belgium

\*dqying@zju.edu.cn

**Abstract:** An analytic model is developed to study the dynamic response of carrier-depletion silicon ring modulators. Its validity is confirmed by a detailed comparison between the modeled and the measured small signal frequency response of a practical device. The model is used to investigate how to maximize the optical modulation amplitude (OMA) and how the OMA could be traded for the bandwidth by tuning the coupling strength and the operation wavelength. Our calculation shows that for a ring modulator with equal RC time constant and photon lifetime, if its operation wavelength shifts from the position of the maximum OMA towards the direction that is away from the resonance, the 3dB modulation bandwidth increases ~2.1 times with a penalty of 3 dB to the OMA.

©2014 Optical Society of America

OCIS codes: (230.4110) Modulators; (230.5750) Resonators.

## References and links

1. X. Xiao, X. Li, H. Xu, Y. Hu, K. Xiong, Z. Li, T. Chu, J. Yu, and Y. Yu, "44 Gb/s silicon microring modulators based on zigzag PN junctions," *IEEE Photon. Technol. Lett.* **24**(19), 1712–1714 (2012).
2. X. Xiao, H. Xu, X. Li, Y. Hu, K. Xiong, Z. Li, T. Chu, Y. Yu, and J. Yu, "25 Gbit/s silicon microring modulator based on misalignment-tolerant interleaved PN junctions," *Opt. Express* **20**(3), 2507–2515 (2012).
3. J. C. Rosenberg, W. M. J. Green, S. Assefa, D. M. Gill, T. Barwicz, M. Yang, S. M. Shank, and Y. A. Vlasov, "A 25 Gbps silicon microring modulator based on an interleaved junction," *Opt. Express* **20**(24), 26411–26423 (2012).
4. A. Biberman, E. Timurdogan, W. A. Zortman, D. C. Trotter, and M. R. Watts, "Adiabatic microring modulators," *Opt. Express* **20**(28), 29223–29236 (2012).
5. P. Dong, S. Liao, D. Feng, H. Liang, D. Zheng, R. Shafiiha, C. C. Kung, W. Qian, G. Li, X. Zheng, A. V. Krishnamoorthy, and M. Asghari, "Low V<sub>pp</sub>, ultralow energy, compact, high-speed silicon electro-optic modulator," *Opt. Express* **17**(25), 22484–22490 (2009).
6. P. Dong, S. Liao, H. Liang, W. Qian, X. Wang, R. Shafiiha, D. Feng, G. Li, X. Zheng, A. V. Krishnamoorthy, and M. Asghari, "High-speed and compact silicon modulator based on a racetrack resonator with a 1 V drive voltage," *Opt. Lett.* **35**(19), 3246–3248 (2010).
7. G. Li, X. Zheng, J. Yao, H. Thacker, J. Shubin, Y. Luo, K. Raj, J. E. Cunningham, and A. V. Krishnamoorthy, "25 Gb/s 1 V driving CMOS ring modulator with integrated thermal tuning," *Opt. Express* **19**(21), 20435–20443 (2011).
8. B. Guha, K. Preston, and M. Lipson, "Athermal silicon microring electro-optic modulator," *Opt. Lett.* **37**(12), 2253–2255 (2012).
9. H. Yu, M. Pantouvaki, S. Dwivedi, P. Verheyen, G. Lepage, R. Baets, W. Bogaerts, and J. Van Campenhout, "Compact thermally tunable silicon racetrack modulators based on an asymmetric waveguide," *IEEE Photon. Technol. Lett.* **25**(2), 159–162 (2013).
10. P. Dong, R. Shafiiha, S. Liao, H. Liang, N. N. Feng, D. Feng, G. Li, X. Zheng, A. V. Krishnamoorthy, and M. Asghari, "Wavelength-tunable silicon microring modulator," *Opt. Express* **18**(11), 10941–10946 (2010).
11. W. D. Sacher, W. M. J. Green, S. Assefa, T. Barwicz, H. Pan, S. M. Shank, Y. A. Vlasov, and J. K. S. Poon, "Coupling modulation of microrings at rates beyond the linewidth limit," *Opt. Express* **21**(8), 9722–9733 (2013).
12. M. Pantouvaki, H. Yu, M. Rakowski, P. Christie, P. Verheyen, G. Lepage, N. Van Hoovels, P. Absil, and J. Van Campenhout, "Comparison of silicon ring modulators with interdigitated and lateral PN junctions," *IEEE J. Sel. Top. Quantum Electron.* **19**(2), 7900308 (2013).

13. W. D. Sacher and J. K. Poon, "Dynamics of microring resonator modulators," *Opt. Express* **16**(20), 15741–15753 (2008).
14. L. Zhang, Y. Li, J. Yang, M. Song, R. G. Beausoleil, and A. E. Willner, "Silicon-based microring resonator modulators for intensity modulation," *IEEE J. Sel. Top. Quantum Electron.* **16**(1), 149–158 (2010).
15. T. Ye and X. Cai, "On power consumption of silicon-microring-based optical modulators," *J. Lightwave Technol.* **28**(11), 1615–1623 (2010).
16. L. Zhang, Y. Li, M. Song, J. Yang, R. G. Beausoleil, and A. E. Willner, "Silicon microring-based signal modulation for chip-scale optical interconnection," *Appl. Phys., A Mater. Sci. Process.* **95**(4), 1089–1100 (2009).
17. B. E. Little, S. T. Chu, H. A. Haus, J. Foresi, and J. P. Laine, "Microring resonator channel dropping filters," *J. Lightwave Technol.* **15**(6), 998–1005 (1997).
18. G. Ghione, *Semiconductor Devices for High-speed Optoelectronics* (Cambridge, 2009), Chap. 6.
19. A. Masood, M. Pantouvaki, D. Goossens, G. Lepage, P. Verheyen, D. Van Thourhout, P. Absil, and W. Bogaerts, "CMOS-compatible tungsten heaters for silicon photonic waveguides," *Proc. 9th IEEE International Conference on Group IV Photonics*, 234–236 (2012).
20. T. Baba, S. Akiyama, M. Imai, N. Hirayama, H. Takahashi, Y. Noguchi, T. Horikawa, and T. Usuki, "50 Gb/s ring-resonator-based silicon modulator," *Opt. Express* **21**(10), 11869–11876 (2013).
21. J. Van Campenhout, M. Pantouvaki, P. Verheyen, S. Selvaraja, G. Lepage, H. Yu, W. Lee, J. Wouters, D. Goossens, M. Moelants, W. Bogaerts, and P. Absil, "Low-voltage, Low-loss, Multi-Gb/s silicon micro-ring modulator based on a MOS capacitor," *Proc. Optical Fiber Communication Conference, OFC 2012*, 4 (2012).
22. M. Gould, T. Baehr-Jones, R. Ding, S. Huang, J. Luo, A. K. Y. Jen, J. M. Fedeli, M. Fournier, and M. Hochberg, "Silicon-polymer hybrid slot waveguide ring-resonator modulator," *Opt. Express* **19**(5), 3952–3961 (2011).
23. A. Ayazi, T. Baehr-Jones, Y. Liu, A. E. Lim, and M. Hochberg, "Linearity of silicon ring modulators for analog optical links," *Opt. Express* **20**(12), 13115–13122 (2012).

## 1. Introduction

Carrier-depletion silicon micro-ring/disk modulators have been studied quite extensively during the past few years, largely because of their advantages such as CMOS compatibility, ultralow power consumption, high operation speed, compact footprint, and so on. All these merits are highly desired by the optical interconnect technology for future data centers and high performance computing systems. Although many modulators of this type have been successfully demonstrated to fully exploit their inherent advantages [1–6], and to overcome their drawbacks like thermal sensitivity [7–10] and modulation bandwidth limitation imposed by the cavity photon lifetime [11], the mechanism to determine their dynamic response is still not thoroughly investigated. For example, when it comes to the 3 dB modulation bandwidth, a widely used formula is  $1/f_{3\text{dB}}^2 = 1/f_Q^2 + 1/f_{\text{RC}}^2$ , where  $f_Q$  and  $f_{\text{RC}}$  are the bandwidth limitations imposed by the cavity photon lifetime and the RC time constant of the device, respectively [3, 5, 12]. However, it has been observed that silicon ring modulators can operate at speeds beyond the predictions of this formula. For example, in [3] the calculation based on the measured quality factor  $Q$ , low frequency resistance, and capacitance gives a 3 dB modulation bandwidth of  $f_{3\text{dB}} = 19$  GHz intrinsically, or 7.2 GHz when combined with the 50  $\Omega$  impedance of the pattern generator. In contrast, eye diagram is obtained up to 40 Gb/s. Also,  $f_{3\text{dB}}$  is calculated to be around 25 GHz in [1], whilst eyes diagrams at 20 Gb/s and 44 Gb/s present extinction ratios (ER) of 3.4 dB and 3 dB, respectively, using a voltage swing of 3 V and a DC bias of –3 V. There have been some preliminary reports revealing that the modulation bandwidth depends also on the optical carrier wavelength [1, 13, 14], a factor that is not included in the aforementioned formula.

Several theoretical models have been developed to analyze the dynamic behavior of the ring modulator. W. D. Sacher gives a rigorous closed-form solution to the small signal frequency response of the ring modulator by building a time-dependent micro-ring transmission model [13]. In this model, the circuit used to electrically represent the device is not incorporated. Therefore, the motion of electrons is ignored and only the dynamics of photons are modeled. On the other hand, the model assumes a pure index or loss modulation. However, the index modulation is always accompanied by a propagation loss modulation for practical devices based on the plasma dispersion effect. An alternative model developed by T. Ye utilizes the mode coupling theory in time domain [15]. Similar to W. D. Sacher's work, T. Ye's model considers neither the response of electrons nor the accompanying loss modulation. Moreover, two more assumptions are made so as to deduce a closed-form expression of the frequency response, i.e., the ring should be critically coupled, and the

wavelength of the optical carrier should be exactly at resonance. The same coupling theory of modes in time domain is employed to compare the performances of different ring configurations by L. Zhang [14, 16], who solves the model numerically by using the implicit Euler method. In general, the above theoretical analyses are based on simplified models, and therefore cannot offer a full and accurate picture about how electrons modulate photons in a silicon ring modulator. It is noteworthy that these models are validated by any measurement result.

In this paper, we study the bandwidth of carrier-depletion silicon ring modulators by establishing a fully analytic model. The model enables a rigorous closed-form expression to describe the small-signal frequency-response of the device. Compared with the previous works [13–16], neither does the model neglect any practical factors which could impact the electrical-optical (EO) modulation, such as the response of the circuit and the loss modulation, nor does it make limitations to the operation conditions such as the coupling condition and the operation wavelength. Moreover, its effectiveness is confirmed by the measurement result of a practical device. Based on this model, relevant elements that determine the speed of silicon ring modulators are investigated. The paper is organized as follows: at first, the model is developed in section II by leveraging the coupling theory of modes in time domain, and then an analytical closed-form solution is deduced successfully. After that, the model is used to calculate the small-signal frequency response of a practical ring modulator. The calculation is compared with the measured data so as to validate the model. This part is in section III of the paper. With the model being proved to be effective, we systematically study the frequency response of silicon ring modulators in section IV. Emphasis is made on how the optical modulation amplitude (OMA) can be traded for the bandwidth. Finally, we summarize the paper in section V.

## 2. Dynamic model of carrier-depletion silicon ring modulators

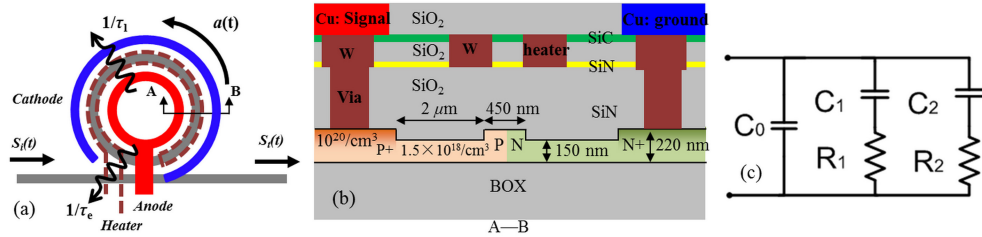


Fig. 1. (a) Schematic diagram of a typical carrier-depletion ring modulator with an integrated heater. (b) Cross-section of the rib waveguide. (c) Equivalent circuit of the device.

A schematic diagram of a typical carrier-depletion silicon ring modulator is shown in Fig. 1(a). The rib waveguide forming the all-pass ring is embedded with a lateral PN junction where a voltage signal is applied to control the resonance wavelength. Under the small signal regime, the electrical behavior of the device can be modeled effectively by its equivalent circuit. The most prevailing circuit so far [1, 2, 7] is shown in Fig. 1(c):  $C_0$ ,  $C_1$ , and  $C_2$  denote the capacitances of the contact pad, the reverse-biased PN junction and the buried oxide layer, respectively, while  $R_1$  and  $R_2$  denote the resistances of the PN junction and the silicon substrate, respectively. Supposing an external voltage signal of  $v_0 \cos(\omega_1 t)$  is applied on the device, the AC voltage across the PN junction is

$$v_{pn}(\omega_1) = v_0 f(\omega_1) \cos[\omega_1 t + \phi(\omega_1)] \quad (1)$$

where  $f(\omega_1)$  and  $\phi(\omega_1)$  are the relative modulus and argument of  $v_{pn}(\omega_1)$  with respect to the external driving signal, respectively

$$f(\omega_1) = \left| \frac{Z_{\text{DUT}}}{Z_{\text{DUT}} + 50} \cdot \frac{1}{1 + j\omega_1 R_1 C_1} \right| \quad (2)$$

$$\phi(\omega_1) = \arg\left(\frac{Z_{\text{DUT}}}{Z_{\text{DUT}} + 50} \cdot \frac{1}{1 + j\omega_1 R_1 C_1}\right) \quad (3)$$

In Eqs. (2) and (3), 50  $\Omega$  is the output impedance of the testing system, and  $Z_{\text{DUT}}$  is the impedance of the device

$$Z_{\text{DUT}} = \frac{1}{j\omega_1 C_0} \left\| \left( \frac{1}{j\omega_1 C_1} + R_1 \right) \right\| \left( \frac{1}{j\omega_1 C_2} + R_2 \right) \quad (4)$$

On the other hand, the dynamic behavior of photons circulating inside the ring can be described by the time rate equation [17]

$$\frac{d}{dt} a(t) = (j\omega_0 - \frac{1}{\tau})a(t) - j\mu A e^{j\omega t} \quad (5)$$

where  $a(t)$  represents the amplitude of the total energy stored in the ring,  $A$  and  $\omega$  are the amplitude and the angular frequency of the incident optical carrier, respectively,  $\omega_0$  is the angular resonance frequency of the ring. The optical field inside the ring decays as a result of the coupling with the bus waveguide and the propagation loss of the doped rib waveguide. The corresponding amplitude decay rates are denoted as  $1/\tau_e$  and  $1/\tau_l$ , respectively. Thus, the overall decay rate is  $1/\tau = 1/\tau_e + 1/\tau_l$ , which is twice the usually referred cavity photon lifetime. The parameter  $\mu$  denotes the mutual coupling between the ring and the bus waveguide. According to the power conservation law, the relationship between  $\mu$  and  $\tau_e$  is  $\mu^2 = 2/\tau_e$  [17]. With the group velocity of the silicon waveguide and the radius of the ring,  $1/\tau_e$  and  $1/\tau_l$  can be easily translated into the cross coupling coefficient between the ring and the bus waveguide and the round trip loss of the ring, respectively [17]. The specific formulas are not listed here for brevity. The transmitted field in the bus waveguide is expressed as

$$S_t(t) = A \exp(j\omega t) - j\mu a(t) \quad (6)$$

The solution of  $S_t(t)$  in static state is

$$S_t = A \frac{j(\omega - \omega_0) + \frac{1}{\tau} - \frac{2}{\tau_e}}{j(\omega - \omega_0) + \frac{1}{\tau}} \exp(j\omega t) \quad (7)$$

To achieve the EO modulation, the motion of free carriers affects that of photons through the plasma dispersion effect. The effect allows the voltage across the PN junction  $v_{\text{pn}}$  to shift the resonance frequency  $\omega_0$  and the amplitude decay rate  $1/\tau$  [12]. In the small signal regime the variations of  $\omega_0$  and  $1/\tau$  depend linearly on  $v_{\text{pn}}(\omega_1)$

$$\omega'_0 = \omega_0 + \frac{\Delta\omega_0}{\Delta v_{\text{pn}}} v_{\text{pn}}(\omega_1) \quad (8)$$

$$\left(\frac{1}{\tau}\right)' = \frac{1}{\tau} + \frac{\Delta(1/\tau)}{\Delta v_{\text{pn}}} v_{\text{pn}}(\omega_1) \quad (9)$$

Here, the rates of change of  $\omega_0$  and  $1/\tau$  with respect to  $v_{\text{pn}}$ , i.e.,  $\Delta\omega_0/\Delta v_{\text{pn}}$  and  $\Delta(1/\tau)/\Delta v_{\text{pn}}$ , are inherent properties of a modulator which are determined by the specific ion implantation

condition, doping pattern, waveguide geometry, bias condition, and so on. Substituting Eqs. (8) and (9) into (5), we get the time-rate equation for carrier-depletion based ring modulators

$$\frac{d}{dt}a(t) = \left\{ \left( j\omega_0 - \frac{1}{\tau} \right) + jv_0 K_{pn} f(\omega_1) \cos[\omega_1 t + \phi(\omega_1)] \right\} a(t) - j\mu A e^{j\omega t} \quad (10)$$

The coefficient  $K_{pn}$  in Eq. (10) is defined as  $K_{pn} = \Delta\omega_0/\Delta v_{pn} + j\Delta(1/\tau)/\Delta v_{pn}$ . The analytic solution for the first-order differential equation in Eq. (10) is

$$a(t) = -j\mu A \exp \left\{ \left( j\omega_0 - \frac{1}{\tau} \right) t + jv_0 K_{pn} \frac{f(\omega_1)}{\omega_1} \sin[\omega_1 t + \phi(\omega_1)] \right\} \\ \times \int \exp \left\{ j(\omega - \omega_0)t + \frac{t}{\tau} - jv_0 K_{pn} \frac{f(\omega_1)}{\omega_1} \sin[\omega_1 t + \phi(\omega_1)] \right\} dt \quad (11)$$

To calculate the integral in Eq. (11), we use the Jacobi-Anger expansion:  $\exp(jz\sin\theta) = \sum J_n(z)\exp(jn\theta)$ , where  $J_n(z)$  is the  $n$ -th Bessel function. After some algebra, we get the closed-form expression of  $a(t)$

$$a(t) = -j\mu A \exp \left[ \left( j\omega_0 - \frac{1}{\tau} \right) t \right] \sum_{n=-\infty}^{+\infty} J_n \left[ v_0 K_{pn} \frac{f(\omega_1)}{\omega_1} \right] \exp[jn(\omega_1 t + \phi(\omega_1))] \\ \times \sum_{m=-\infty}^{+\infty} J_m \left[ -v_0 K_{pn} \frac{f(\omega_1)}{\omega_1} \right] \frac{\exp \left[ j(\omega - \omega_0 + m\omega_1)t + \frac{t}{\tau} + jm\phi(\omega_1) \right]}{j(\omega - \omega_0 + m\omega_1) + \frac{1}{\tau}} \quad (12)$$

The multiplication between the two summations in Eq. (12) generates high-order harmonics of the modulation frequency  $\omega_1$ . By neglecting high-order harmonics, and then substituting the DC and the first harmonic components into Eq. (6), we have

$$S_i(t) = A \exp(j\omega t) \left\{ \frac{j(\omega - \omega_0) + \frac{1}{\tau} - \frac{2}{\tau_e}}{j(\omega - \omega_0) + \frac{1}{\tau}} - \frac{jv_0 \mu^2 K_{pn} f(\omega_1)}{[j(\omega - \omega_0) + \frac{1}{\tau}]^2 + \omega_1^2} \cos \omega_1 t \right. \\ \left. - \frac{jv_0 \mu^2 K_{pn} f(\omega_1)}{[j(\omega - \omega_0) + \frac{1}{\tau}]^2 + \omega_1^2} \frac{\omega_1 \sin \omega_1 t}{[j(\omega - \omega_0) + \frac{1}{\tau}]} \right\} \quad (13)$$

The following properties of the Bessel function have been utilized as we limit our discussion in the small signal regime:  $J_0(z) \approx 1$ ,  $J_1(z) \approx z/2$ , and  $J_{n>1}(z) \approx 0$  for  $|z| \ll 1$ . The first term inside the braces of Eq. (13) is the static transmitted field in the bus waveguide, i.e., the DC component of the modulated light. The rest two terms represent the amplitude modulation.

According to its definition, the optical modulation amplitude (OMA) is calculated as  $OMA = (|S_t|_{\max}^2 - |S_t|_{\min}^2)^{1/2}$ . It is proportional to the peak-to-peak change of the converted AC photocurrent in the detector. On the other hand, the complex transfer function of a modulator, i.e., the S21 parameter, is the ratio of the harmonic component of the modulated optical power to the input sinusoidal voltage signal [18]. Therefore, if the power of the driving signal is fixed, OMA can be regarded as equivalent to the modulus of the S21 parameter.

Up to now, we have established an analytic model for carrier-depletion silicon ring modulators, with which a closed-form expression of the modulated light is successfully deduced to describe the small-signal transmission. The model requires the following parameters as the input:  $\omega_0$ ,  $1/\tau$ ,  $1/\tau_e$ ,  $\Delta\omega_0/\Delta v_{pn}$ ,  $\Delta(1/\tau)/\Delta v_{pn}$ , and the elements in the circuit of

Fig. 1(c). Experimentally, their values can be extracted by fitting to corresponding measurement results, i.e., the static transmission spectra and the reflection coefficient of the RF signal (the S11 parameter). In the next section, we will verify the model by a comprehensive comparison between the modeled and the measured frequency response of a practical ring modulator.

### 3. Verification of the dynamic model

In this section a typical silicon ring modulator on SOI platform is tested. Schematic diagrams of the top view and the cross section of the device are shown in Figs. 1(a) and 1(b), respectively. The dimension of the rib waveguide is  $450 \text{ nm} \times 220 \text{ nm}$ . In order to share the same silicon patterning steps as the shallow-etched fiber grating coupler, the etching depth of the rib waveguide is  $70 \text{ nm}$ , which supports a radius of  $40 \mu\text{m}$  without much bending loss. The nominal doping concentration of the PN junction is  $1.5 \times 10^{18}/\text{cm}^3$ , while the ohmic contact regions are heavily doped to  $10^{20}/\text{cm}^3$ . The gap between the bus waveguide and the ring is  $500 \text{ nm}$ . The tungsten heater on top of the rib enables an active tuning of the operation wavelength. The device is fabricated by imec's silicon photonics platform on its  $200 \text{ mm}$  CMOS pilot line. More details about the processing can be found in [12] and [19].

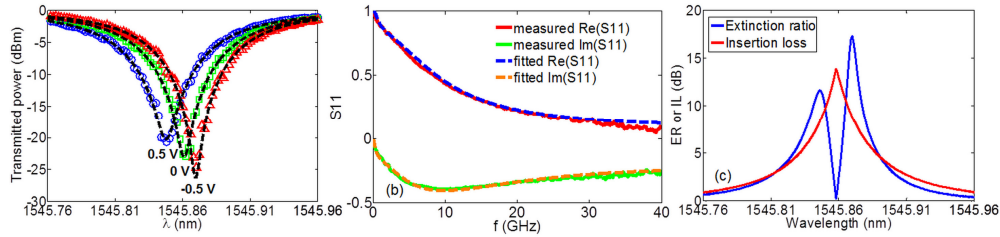


Fig. 2. (a) Transmitted spectra of the ring modulator at different bias voltages. The discrete data points present the measurement result. The black dashed lines are the fitted curves. (b) The S11 parameter of the ring modulator with 0 V bias voltage. The solid and the dashed lines are the measured and the fitted curves, respectively. (c) Extinction ratio and insertion loss for a voltage swing from  $-0.5 \text{ V}$  to  $0.5 \text{ V}$ .

Table 1. Parameters of resonance curves at different bias voltages

Bias Voltage	$\lambda_0$ (nm)	$\omega_0$ (T rad/s)	Q	$1/\tau$ (G rad/s)	$1/\tau_c$ (G rad/s)	$1/\tau_l$ (G rad/s)
0.5 V	1545.848	1219.3671	12540	48.619	21.989	26.63
0 V	1545.861	1219.3565	12900	47.262	21.989	25.273
-0.5 V	1545.870	1219.3497	13200	46.187	21.989	24.198

The measured transmitted spectra of the ring are plotted in Fig. 2(a) as discrete data points for different bias voltages. For each resonance curve we can extract  $\lambda_0$ ,  $\omega_0$ ,  $1/\tau_c$ , and  $1/\tau_l$  by curve fitting according to Eq. (7). The results are listed in Table 1. The fitted curves are shown in Fig. 2(a) as black dashed lines. As a reverse bias is applied, the propagation loss of the doped rib waveguide falls due to the depletion of free carriers, and therefore the corresponding delay rate  $1/\tau_l$  decreases. The data in Table 1 indicates that  $\Delta\omega_0/\Delta v_{pn} = 17.35 \times 10^9 \text{ rad/s/V}$ , and  $\Delta(1/\tau)/\Delta v_{pn} = 2.432 \times 10^9 \text{ rad/s/V}$ . On the other hand, values of the elements in Fig. 1(c) are extracted from the measured S11 parameter of the device, and they are  $C_0 = 20 \text{ fF}$ ,  $C_1 = 170 \text{ fF}$ ,  $C_2 = 400 \text{ fF}$ ,  $R_1 = 75 \Omega$ , and  $R_2 = 1500 \Omega$ . The measured and the fitted S11 curves of the device are displayed in Fig. 2(b) as the solid and the dashed lines, respectively. From Fig. 2(a) we deduce the extinction ratio and the insertion loss versus the wavelength for a voltage swing from  $-0.5 \text{ V}$  to  $0.5 \text{ V}$ , which are presented in Fig. 2(c). The circuit and the Q value of the ring can be translated into an RC time constant and a photon lifetime limited 3 dB bandwidth of  $f_{RC} = 7 \text{ GHz}$  and  $f_{\tau} = 15 \text{ GHz}$ , respectively. A high Q value makes the output of the ring more susceptible to the index variation, which is favorable for enhancing the modulation depth. On the other hand, it imposes a stringent



requirement on the wavelength control and also limits the bandwidth. Most reported ring modulators have their Q values range from 7000 to 15000 for decent overall performances [1–10].

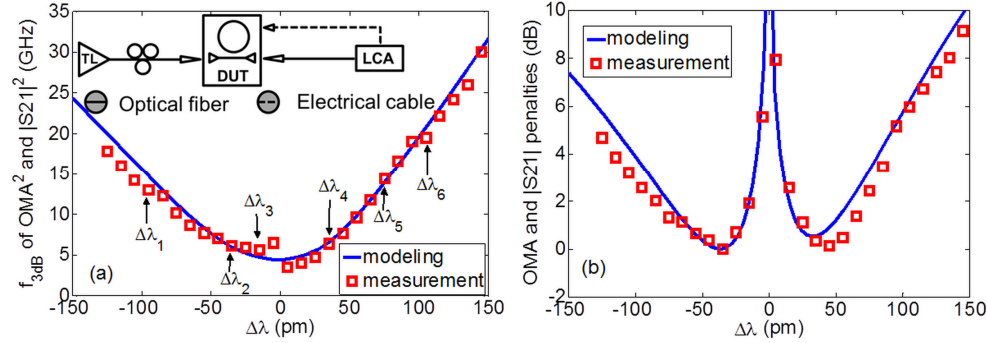


Fig. 3. (a) 3 dB bandwidths of the modeled  $OMA^2$  and the measured  $|S21|^2$  versus the operation wavelength. The inset presents the experiment setup diagram for the S21 parameter measurement. (b) Penalties to the modeled OMA ( $\Delta OMA$ ) and the measured  $|S21|$  at a low modulation frequency of 300 MHz as a function of the operation wavelength. The reverse bias voltage for the two figures is 0 V.  $\Delta\lambda$  is the wavelength offset from the resonance wavelength.

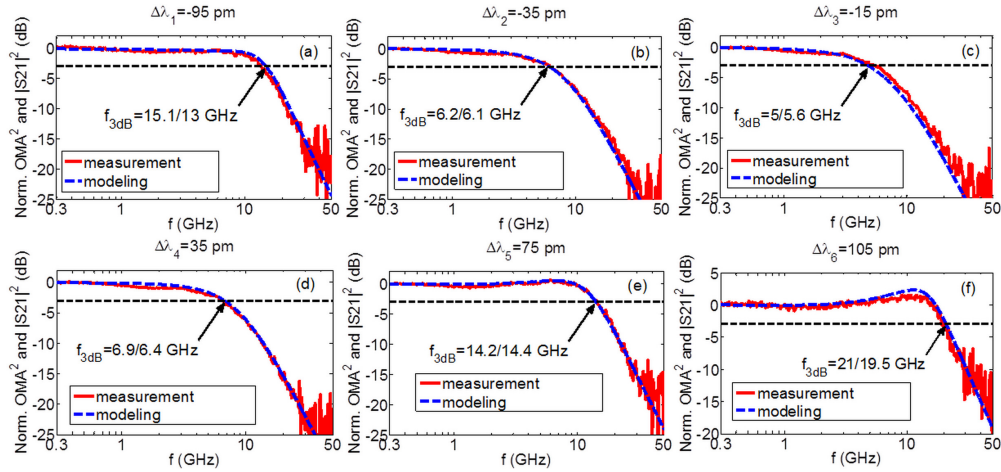


Fig. 4. Frequency responses of the modeled  $OMA^2$  and the measured  $|S21|^2$  at different wavelengths. Both  $OMA^2$  and  $|S21|^2$  are normalized to their values at 300 MHz. The marked values inside the figures are the 3 dB cutoff frequency of  $OMA^2$  and  $|S21|^2$ .

With all necessary parameters ready, the model is used to calculate the small signal frequency response of OMA at different operation wavelengths. Carrier-depletion silicon ring modulators always exhibit higher modulation efficiencies as the reverse bias voltage is low [1–10]. Therefore, all calculations throughout this paper are performed under 0 V reverse bias. An output impedance of 50  $\Omega$  is assumed. Figure 3(a) plots the 3 dB bandwidth of  $OMA^2$  as a function of the carrier wavelength, while Fig. 3(b) presents the wavelength dependence of the OMA penalty ( $\Delta OMA$ ). The OMA penalty is defined as the relative strength of OMA at very low modulation frequency (we use 300 MHz here) with respect to its maximum throughout the full wavelength range in log units, i.e.,  $\Delta OMA = -10 \times \log(OMA/OMA_{\max})|_{\omega=300\text{MHz}}$ .  $\Delta\lambda$  in the two figures denotes the wavelength offset from the resonance wavelength. When the ring is at resonance ( $\Delta\lambda = 0$ ), there is no EO modulation. The two operation bands locate at the two sides of the resonance wavelength. If we consider only the shift of the resonance curve due to the index modulation and neglect the change of its shape due to the loss modulation, the two valleys in Fig. 3(b) correspond to the

wavelengths where the transmission spectrum has the maximum slope. It is apparent from Fig. 3 that the OMA can be traded for bandwidth by tuning the wavelength away from the resonance. By this manner the modulation bandwidth could be increased beyond the limitations due to the RC constant or the photon lifetime at the expense of increased OMA penalty. This will be discussed in detail in the next section.

As aforementioned, the OMA is equivalent to the measurable  $|S_{21}|$  parameter of the device. Therefore, the modeled OMA is compared with the measured  $|S_{21}|$  to validate the model. The small signal frequency response of the  $S_{21}$  parameter of the device under 0 V bias is characterized by a lightwave component analyzer (Agilent N4373D). The measurement is performed through the full spectrum range of interest with a step of 10 pm. The output power of the laser is fixed at 3 dBm. Thereby, the on-chip power is around -5.8 dBm according to the efficiency of the fiber grating coupler. The RF signal is fed to the device through a high speed GSG probe. A schematic diagram of the measurement setup is shown in the inset of Fig. 3(a). The measured 3 dB bandwidth of  $|S_{21}|^2$  and the  $|S_{21}|$  penalty at 300 MHz versus  $\Delta\lambda$  are shown as discrete points in Figs. 3(a) and 3(b), respectively, which show a good agreement with the modeling result.

In order to further validate the model, we also directly compare frequency response curves of the measured  $|S_{21}|^2$  and the modeled OMA<sup>2</sup> in Fig. 4 at different wavelengths. The locations of these wavelengths are marked in Fig. 3(a). Figures 3 and 4 show that the model is effective for studying the dynamic response of carrier-depletion silicon ring modulators.

#### 4. Tradeoff between OMA and modulation bandwidth

With the model established in section 2 and subsequently verified in section 3, in this section we first discuss the property of the EO modulation implemented by silicon carrier-depletion ring modulators, and then explore how OMA could be traded for modulation bandwidth by adjusting the wavelength and the coupling between the ring and the bus waveguide.

##### 4.1 The modulation resonance

It is observed in Fig. 4(f) that the frequency response curve of  $|S_{21}|^2$  presents a peak before the rapid roll-off. Similar phenomenon could be found in Fig. 4(g) as well, despite it is not as discernable as in Fig. 4(f). This can be explained by deducing the expression of  $|S_c(t)|^2$  from Eq. (13). This expression is not listed here for the sake of simplicity. However, it can be found that the coefficient of the first harmonic of  $|S_c(t)|^2$  contains a factor of  $\{[\omega_1^2 + 1/\tau^2 - (\omega - \omega_0)^2]^2 + [2(\omega - \omega_0)/\tau]^2\}^{-1}$ . It is this factor that dominates the roll-off of the final frequency response. If  $|\omega - \omega_0| < 1/\tau$ , this factor and the resultant frequency response are monotonically decreasing functions of  $\omega_1$  as shown in Figs. 4(b)-4(d). However, if  $|\omega - \omega_0| > 1/\tau$ , this factor has a maximum at  $\omega_1 = [(\omega - \omega_0)^2 - 1/\tau^2]^{1/2}$ , which leads to a modulation enhancement as shown in Figs. 4(e) and 4(f). It is noteworthy that the final location of the modulation enhancement could slightly deviate from  $[(\omega - \omega_0)^2 - 1/\tau^2]^{1/2}$  due to the disturbance from other  $\omega_1$  dependent factors in the coefficient of the first harmonic of  $|S_c(t)|^2$ . For example, the blue curve in Fig. 4(f) reaches the maximum at 11.3 GHz. In contrast the value of  $[(\omega - \omega_0)^2 - 1/\tau^2]^{1/2}$  is 10.8 GHz. This phenomenon is referred to as the modulation resonance by W. D. Sacher [13]. He estimates that in the limiting case of a lossless ring, i.e.,  $1/\tau \approx 0$ , the modulation resonance occurs at  $\omega + \omega_1 = 2p\pi/t_0$ , where  $t_0$  is the resonator round-trip time and  $p$  is an integer. Apparently, our model gives the same result for this limiting case.

##### 4.2 The optimum modulation wavelength and coupling condition

Before solving the optimum modulation wavelength, we define it as the wavelength with the maximum OMA at low modulation frequency. As the modulation frequency is low ( $\omega_1 \ll 1/\tau$ ), the amplitude of the sinusoidal signal in Eq. (13) is much smaller than that of the cosine signal and therefore can be neglected. By neglecting also the second order harmonic in  $|S_c(t)|^2$ , we get the expression of OMA at low modulation frequency



$$\text{OMA}|_{\omega_1 \ll 1/\tau} = \left| 4 \text{Re} \left\{ j v_0 A^2 \mu^2 \left[ \frac{\Delta \omega_0}{\Delta v_{\text{pn}}} - j \frac{\Delta(1/\tau)}{\Delta v_{\text{pn}}} \right] f(\omega_1) \right. \right. \\ \left. \left. \times \frac{\left( \frac{1}{\tau} - \frac{2}{\tau_e} \right) \frac{1}{\tau} - (\omega - \omega_0)^2 + j(\omega - \omega_0) \left( \frac{2}{\tau} - \frac{2}{\tau_e} \right)}{[(\omega - \omega_0)^2 + \frac{1}{\tau^2}]^2} \right\} \right| \quad (14)$$

Since the EO modulation mainly relies on the shift of the resonance curve induced by the index modulation  $\Delta(\omega_0)/\Delta v_{\text{pn}}$ , the accompanying loss modulation  $\Delta(1/\tau)/\Delta v_{\text{pn}}$  can be neglected for the first approximation. Thereby, we have

$$\text{OMA}|_{\omega_1 \ll 1/\tau} = \left| 4 v_0 A^2 \mu^2 f(\omega) \frac{\Delta \omega_0}{\Delta v_{\text{pn}}} \frac{(\omega - \omega_0) \left( \frac{2}{\tau} - \frac{2}{\tau_e} \right)}{[(\omega - \omega_0)^2 + \frac{1}{\tau^2}]^2} \right| \quad (15)$$

It can be found that the maximums of Eq. (15) locate at  $\omega = \omega_0 \pm (3^{1/2}\tau)^{-1}$ , which can be translated to wavelengths of  $\lambda = \lambda_0 \pm \lambda_{\text{FWHM}}/2/3^{1/2}$ . Here  $\lambda_{\text{FWHM}}$  is the full width at half maximum of the resonance lineshape. These two wavelengths correspond to the two valleys of Fig. 3(b).

In addition to the optimum operation wavelength, we further deduce the optimum coupling condition to achieve a high OMA. This is implemented by calculating OMA at the optimum wavelength. Substituting the optimum angular frequency of  $\omega = \omega_0 \pm (3^{1/2}\tau)^{-1}$  into Eq. (15), we have  $\text{OMA}|_{\omega_1 \ll 1/\tau} \propto (\tau_1^{1/3} \tau_e^{-2/3} + \tau_e^{1/3} \tau_1^{-2/3})^{-1}$ . Basically,  $\tau_1$  depends on the dopant density and distribution which is determined by the ion implantation condition, and also depends on the sidewall roughness which is determined by the dry etching recipe. Therefore,  $\tau_1$  is processing related and could be regarded as fixed once a standard CMOS processing flow is established. In contrast,  $\tau_e$  is determined by the gap between the ring and the bus waveguide. It can be tuned in the design phase so as to maximize the OMA. The term  $(\tau_1^{1/3} \tau_e^{-2/3} + \tau_e^{1/3} \tau_1^{-2/3})^{-1}$  reaches the maximum provided that  $\tau_e = 2\tau_1$ . This implies that the ring should be under coupled rather than critically coupled for a high OMA.

#### 4.3 The tradeoff between $\Delta\text{OMA}$ and $f_{3\text{dB}}$

The modulation bandwidth  $f_{3\text{dB}}$  and the OMA are two key figures of merit for any modulators, since they indicate the speed and the efficiency of EO modulation, respectively. The two factors are independent of each other for Mach-Zehnder modulators. However, the resonance nature correlates these two factors in optical cavity based modulators such as rings. In this subsection, we discuss this relationship and the mechanism behind it.

Before exploring the relationship between  $f_{3\text{dB}}$  and the OMA, we calculate  $f_{3\text{dB}}$  of the ring modulator with our model. For a long time, the empirical formula  $1/f_{3\text{dB}}^2 = 1/f_Q^2 + 1/f_{\text{RC}}^2$  is used to calculate the modulation bandwidth [3, 5, 12]. Here  $f_Q$  is calculated as  $f_Q = (\pi\tau)^{-1}$ . This formula is an approximation of  $f_{3\text{dB}}$ , since it does not include the impact of coupling condition and operation wavelength. This point is illustrated by the contrast of Fig. 5, where we calculate  $f_{3\text{dB}}/f_Q$  vs.  $f_{\text{RC}}/f_Q$  for different coupling conditions with our model. We use  $f_Q$  to normalize both  $f_{3\text{dB}}$  and  $f_{\text{RC}}$  so as to make the result universal for rings of different quality factors. In the calculation, the device operates at its optimum wavelength deduced in section 4.2. The black dashed line presents the calculation result with the empirical formula. For an ideal ring at the optimum coupling and operation wavelength, i.e., the red curve in Fig. 5, its

practical bandwidth is around 61% of that predicted by the **empirical** formula. This correction factor is around 77% for a critical coupled ring modulator.

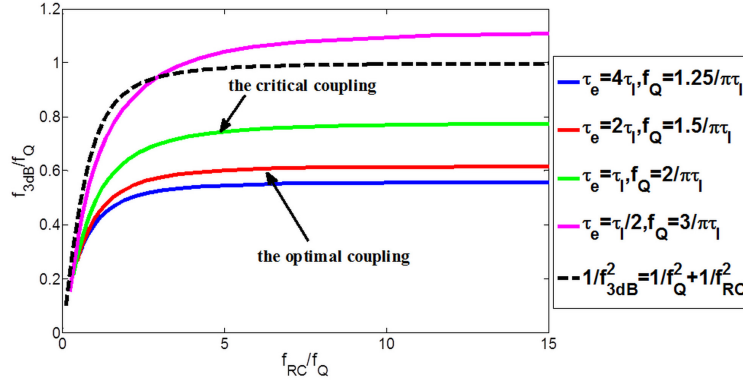


Fig. 5.  $f_{3dB}/f_Q$  as a function of  $f_{RC}/f_Q$  for different coupling conditions. The device works at the optimum wavelength of  $\lambda = \lambda_0 \pm \lambda_{FWHM}/2/3^{1/2}$  during the modeling.

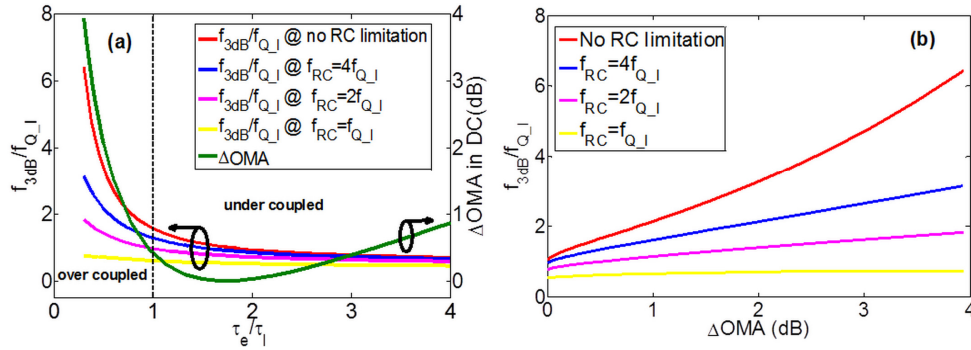


Fig. 6. (a)  $f_{3dB}/f_{Q,1}$  and  $\Delta OMA$  as a function of  $\tau_e/\tau_1$  for different RC constants. (b) the relationships between  $f_{3dB}/f_{Q,1}$  and  $\Delta OMA$  for different RC constants. The device works at the optimum wavelength which is calculated as  $\lambda_0 - \lambda_{FWHM}/2/3^{1/2}$ . The penalty to OMA is induced by reducing  $\tau_e$  (increasing the coupling between the ring and the bus waveguide) from  $\tau_e/\tau_1 \approx 1.7$ .

The red curve of Fig. 5 gives the bandwidth of the ring modulator with the maximum OMA. The high OMA then can be traded for the bandwidth. As aforementioned,  $\tau_1$  and the RC time constant of the device depend on the practical processing. Therefore, the parameters that can be tuned freely to implement the tradeoff are  $\tau_e$  and  $\omega$ . The 3 dB bandwidth  $f_{3dB}$  and the penalty to the OMA, i.e.,  $\Delta OMA$ , are plotted in Fig. 6(a) as a function of  $\tau_e/\tau_1$  for different RC constants.  $f_{Q,1}$  is the bandwidth corresponding to the intrinsic quality factor of the ring  $f_{Q,1} = (\pi\tau_1)^{-1}$  and it is used to normalize  $f_{3dB}$  and  $f_{RC}$ . We do not use  $f_Q$  for the frequency normalization here. The reason is that  $f_Q$  is a variable when we change  $\tau_e$ . The case of “no RC limitation” in Fig. 6(a) implies that we didn’t consider any limitation due to the RC constant, which is  $f_{RC} = +\infty$ . The device is assumed to operate at the optimum wavelength deduced in section 4.2 throughout the calculation of Fig. 6(a). The maximum OMA, i.e.,  $\Delta OMA = 0$ , occurs at  $\tau_e/\tau_1 \approx 1.7$ . This is slightly smaller than the expected value of  $\tau_e/\tau_1 = 2$ . The reason for this discrepancy is that we have neglected the loss modulation  $\Delta(1/\tau)/\Delta v_{pn}$  in section 4.2. As we reduce  $\tau_e$  from the optimum value by increasing the coupling strength between the ring and the bus waveguide, both  $f_{3dB}$  and  $\Delta OMA$  increase. In this manner OMA could be traded for the bandwidth. The relationship between  $\Delta OMA$  and  $f_{3dB}$  are extracted from Fig. 6(a) for different RC constants and displayed in Fig. 6(b).

Compared with tuning  $\tau_e$  in the design phase, a much more flexible way to trade OMA for  $f_{3dB}$  is to adjust the operation wavelength. The dependences of  $f_{3dB}/f_Q$  and  $\Delta OMA$  on  $(\lambda - \lambda_0)$

$/\lambda_{FWHM}$  are plotted in Fig. 7(a) for different RC constants. The coupling condition of  $\tau_c = 2\tau_1$  is utilized in the calculation. Similar to Fig. 6(a), the final optimum wavelength of  $(\lambda - \lambda_0) / \lambda_{FWHM} = -0.32$  in Fig. 7(a) slightly deviates from the theoretical estimation of  $(\lambda - \lambda_0) / \lambda_{FWHM} = -1/2/3^{1/2} \approx -0.28$  since the loss modulation is neglected in section 4.2. Figure 7(b) presents the extracted correspondence between  $f_{3dB}/f_Q$  and  $\Delta OMA$  while  $\lambda$  is shifted towards shorter wavelengths from the optimum position (away from the resonance). Figure 7 indicates that the achievable bandwidth of a practical ring modulator could be substantially higher than the bandwidth limitation imposed by the photon lifetime or the RC constant, as long as one can tolerate a low OMA or a high driving voltage. If  $f_Q = f_{RC}$ , a 3 dB penalty to OMA can boost the modulation bandwidth by a factor of  $\sim 2.1$  in Fig. 7(b). This is from  $f_{3dB} = 0.45 \times f_Q$  at  $\Delta OMA = 0$  to  $f_{3dB} = 0.97 \times f_Q$  at  $\Delta OMA = 3$  dB. It can be seen from Figs. 6(b) and 7(b) that a reduced RC constant could make the trade between  $f_{3dB}$  and  $\Delta OMA$  more efficient.

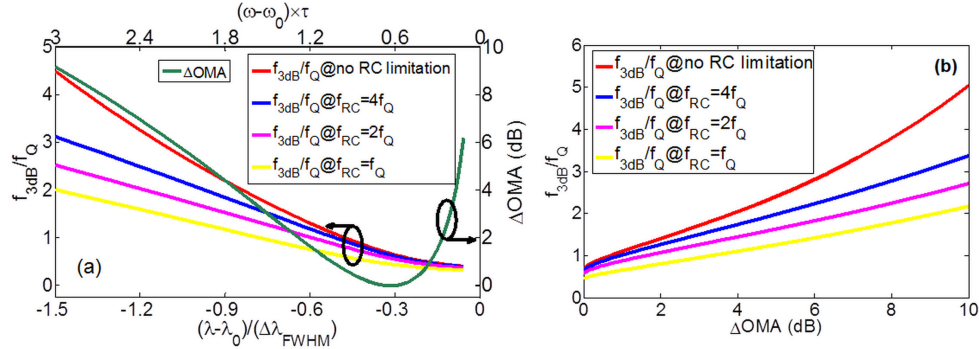


Fig. 7. (a)  $f_{3dB}/f_Q$  and  $\Delta OMA$  as a function of  $(\lambda - \lambda_0) / \lambda_{FWHM}$  for different RC constants. (b) The relationships between  $f_{3dB}/f_Q$  and  $\Delta OMA$  for different RC constants. The device works at the coupling condition of  $\tau_c = 2\tau_1$ . The penalty to OMA is induced by reducing the wavelength from  $(\lambda - \lambda_0) / \lambda_{FWHM} = -0.32$ .

The penalty to OMA could be eliminated by magnifying the driving voltage. Therefore, the calculation in this subsection also indicates how a high driving voltage enables a ring modulator to operate faster.

## 5. Conclusion

In this paper an analytic model is established to describe the dynamic behavior of carrier-depletion silicon ring modulators. The model was compared and validated with extensive small-signal frequency response measurements on a typical ring modulator. The model was then used to investigate the relationship between OMA and  $f_{3dB}$ . Measures to increase the modulation bandwidth together with the corresponding penalty in OMA are explored. The model was developed for devices utilizing the carrier-depletion effect of the PN junction. However, it is applicable to devices based on other mechanisms, such as the carrier-injection effect of the PIN diode [20], the carrier-accumulation effect of the MOS capacitor [21], the electro-optical effect of polymer [22], and so on, as long as the equivalent circuit to describe the motion of electrons is adjusted accordingly. The discussion in this work is restricted in the small signal regime. However, the model can be extended to the large signal regime provided that the nonlinearity of the EO modulation is taken into account. It implies  $\omega'_0$  and  $(1/\tau)'$  in Eqs. (8) and (9) are no more linearly dependent on  $v_{pn}$ . The quadratic terms have to be included [23]. On the other hand, the ring modulators of the state of the art only require a driving voltage of  $\sim 1$  V [6, 7, 12]. They almost operate in the small signal regime under such a low driving voltage. Therefore, the conclusions in this paper still hold true. In a word, the result of this paper can help designers and optical test engineers to understand the potential and the boundary of the performance of a specific silicon ring modulator.

## **Acknowledgment**

This work is supported by the Natural Science Foundations of China (No. 61177055 and No. 61307074), the Nature Basic Research Program of China (No.2013CB632105), and the Fundamental Research Funds for the Central Universities of China.